Topological properties of nearly flat bands in bilayer $\alpha - T_3$ lattice

Puspita Parui [*], Sovan Ghosh,[†] and Bheema Lingam Chittari [‡]

Department of Physical Sciences, Indian Institute of Science Education and Research Kolkata, Mohanpur 741246, West Bengal, India

We study the effect of Haldane flux in the bilayer α-$\mathcal{T}_3$ lattice system, considering possible nonequivalent, commensurate stacking configurations with a tight-binding formalism. The bilayer α-$\mathcal{T}_3$ lattice comprises six sublattices in a unit cell, and its spectrum consists of six bands. In the absence of Haldane flux, threefold band crossings occur at the two Dirac points for both valence and conduction bands. The introduction of Haldane flux in a cyclically stacked bilayer α-$\mathcal{T}_3$ lattice system separates all six bands, including two low-energy, corrugated nearly flat bands, and assigns nonzero Chern numbers to each band, rendering the system topological. We demonstrate that the topological evolution can be induced by modifying the hopping strength between sublattices with the scaling parameter α in each layer. In the dice lattice limit ($\alpha = 1$) of the Chern-insulating phase, the Chern numbers of the three pairs of bands, from low energy to higher energies, are ± 2, ± 3, and ± 1. Interestingly, a continuous change in the parameter α triggers a topological phase transition through band crossings between the two lower energy valance and conduction band. These crossings occur at different values for two different BZ-points and depend further on the next-nearest-neighbor hopping strength. Moreover, there are multiple topological phase transitions are found for $0 < \alpha < 1$.

I. INTRODUCTION

The discovery of unconventional superconductivity in twisted-bilayer graphene (TBG) [1] has ignited significant interest in identifying flat bands in 2D materials [2]. In magic-angle TBG, flat bands are not isolated unless subjected to a staggered potential and an external electric field [3]. However, new proposals, such as twisted double bilayer graphene and multilayer graphene aligned on boron nitride, exhibit isolated flat bands under an external electric field [4–16]. These gate-tunable isolated flat bands have been found to possess topological properties [4–16]. The nontrivial flat band topology inherently leads to a rich spectrum of physical phenomena driven by Coulomb interactions, which are proportional to the reduced kinetic energy. Moreover, topological flat bands have enabled the observation of phenomena such as superconductivity [17], excitonic insulator states [18,19], fractional quantum anomalous Hall effects [20–22], ferromagnetism [23,24], and excited quantum anomalous or spin Hall effects [25]. In addition to TBG, flat bands are observed in kagome [26,27], $\mathcal{T}_3$ or dice [28,29], and Lieb lattices [30,31]. The $\mathcal{T}_3$ or dice lattice exhibits flat bands near charge neutrality due to destructive interference of wave functions, resulting in electronic bands without dispersion [2,32–34]. These flat bands are trivial in nature with nonsingular Bloch wave functions [2,32–34]. Experimental realization of the dice lattice was proposed and discussed using an optical lattice, utilizing three pairs of counterpropagating identical laser beams

with the same wavelength of $\lambda = \frac{3}{2a}$, where a is the lattice constant, and a Josephson Junction array [35,36]. This was followed by another proposal for the experimental realization of the dice lattice using artificial heterostructures of trilayer cubic lattices grown along the (111) direction, such as $SrTiO_3/SrIrO_3/SrTiO_3$ [37]. α-$\mathcal{T}_3$ shows a continuously variable Berry phase from π (graphene) to 0 (dice) with the variable α, and the Berry phase dependence of quantized Hall conductivity, dynamical longitudinal optical conductivity, and Shubnikov–de Haas oscillation has been established [38]. The effect of the variable Berry phase on the orbital magnetic susceptibility of α-$\mathcal{T}_3$ with the variation of α is observed [39]. Further, the magnetotransport property of α-$\mathcal{T}_3$ has been studied, and it is found that the Hall conductivity undergoes a smooth transition from $\sigma_{yx} = 2(2n + 1)(e^2/h)$ to $\sigma_{yx} = 4n(e^2/h)$ with $n = 0, 1, 2, \ldots$ as α is tuned from 0 to 1 [40]. The effect of disorder and staggered lattice potential on integer quantum Hall plateaus has been established [41]. Floquet states and the variable Berry-phase-dependent photoinduced gap in the α-$\mathcal{T}_3$ lattice irradiated by circularly polarized on-resonant light have been studied [42]. Later, the Floquet topological phase transition in a single-layer α-$\mathcal{T}_3$ lattice was shown by breaking of time-reversal symmetry (TRS) using off-resonant circularly polarized light and varying α discovered the topological phase transition ($C_n = 2$ to $C_n = 1$) at $\alpha = \frac{1}{\sqrt{2}}$ [43]. More recently, higher Chern numbers have been observed in the single-layer dice lattice. A Haldane-like model on the dice lattice (single-layer) showed Chern numbers of the three bands ± 2 (dispersive valence band and conduction band) and 0 (flat band in the middle). Also, the quantum anomalous Hall effect with two chiral channels per edge was observed [44]. A topological phase transition from Chern insulating ($\sigma_{xy} = 2e^2/h$) to a trivial ($\sigma_{xy} = 0$) insulating

*puspitaparui44@gmail.com
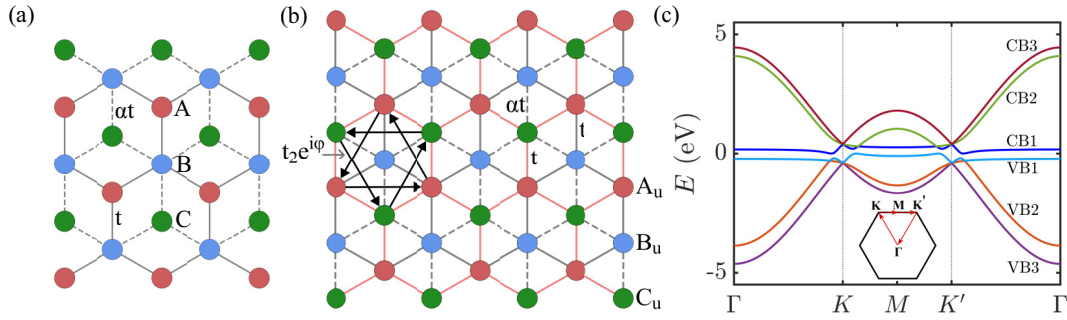†sovanghosh2014@gmail.com
‡bheemalingam@iiserkol.ac.in

FIG. 1. (a) Schematic diagram of single-layer α-$\mathcal{T}_3$ lattice. (b) Schematic diagram (top view) of cyclically stacked bilayer α-$\mathcal{T}_3$ lattice; positions of sites A_u (C_l), B_u (A_l), and C_u (B_l) of the upper (lower) layer denoted by red, green, and blue, respectively. The NN hopping of the upper and lower layers are denoted as gray and red lines, and the hopping strength between sites B and C are shown as αt (dashed) and between B and A (solid) as t. The next NNN complex hopping of strength $t_2 e^{i\phi}$ for A and C sublattices is shown with black arrows for anticlockwise direction. (c) Band structure of cyclically ($A_l B_u$-$B_l C_u$-$C_l A_u$) stacked bilayer α-$\mathcal{T}_3$ lattice, calculated along the path of high symmetry points (Γ-K-M-K'-Γ) in the absence of Haldane flux and the path in the hexagonal Brillouin zone (inset).

phase was observed at the semi-Dirac limit of the dice lattice [45].

However, the flat bands near the charge neutrality in the α-$\mathcal{T}_3$ lattice become dispersive at the band-touching high-symmetric point (K and K') in the presence of spin-orbit coupling and become nontrivial [37]. Interestingly, when two layers of the α-$\mathcal{T}_3$ lattice stack on top of each other to form a bilayer with four nonequivalent commensurate stacking, the effective low-energy model shows the dispersive nature of the flat bands near the charge neutrality [46]. The topological properties of these nearly flat bands of bilayer α-$\mathcal{T}_3$ lattices have not been explored.

This paper is organized in the following way. In Sec. II we presented the model Hamiltonian of the bilayer system. In Sec. III we discuss the results, where Sec. III A shows the spectral properties for different stacking configurations, and Secs. III B and III C present the topological properties and show the Chern phase diagrams. Further, in Sec. III D we present the anomalous Hall conductivity. We finally conclude with a brief summary of the results obtained in Sec. IV.

II. THE MODEL HAMILTONIAN

A. Single-layer and bilayer α-$\mathcal{T}_3$ lattice

The α-$\mathcal{T}_3$ lattice is similar to a honeycomb lattice but with an additional lattice site at the center of the hexagon, as shown in Fig. 1(a). The two sublattice sites, A and B, form the honeycomb lattice with a nearest-neighbor (NN) hopping amplitude of t (solid line). Additionally, the third sublattice site, C, located at the center of the hexagon, connects to site B with NN hopping, and the hopping amplitude can be tuned with a parameter α, defined as αt (dashed line). This lattice structure is bipartite, with sites A and C referred to as "rim atom" sites, and the B lattice sites are known as "hub atom" sites. The rim atoms have 3 nearest neighbors, whereas hub atoms have 6 nearest neighbors [28,29,35,36,47–50]. The real parameter α smoothly interpolates between two limiting cases of the model, $\alpha = 0$ and 1, referred to as graphene and the dice lattice, respectively. The intermediate values, $0 < \alpha < 1$, are defined as the α-$\mathcal{T}_3$ lattice [39]. In this paper, we discuss

the bilayer structure of the α-$\mathcal{T}_3$ lattices. The α-$\mathcal{T}_3$ bilayer has four nonequivalent vertically aligned commensurate stackings [46]. The two layers stack on top of each other, where each sublattice (A_u, B_u, C_u) from the top layer aligns exactly on top of each sublattice (A_l, B_l, C_l) of the bottom layer; this is called "aligned" ($A_l A_u$-$B_l B_u$-$C_l C_u$). A $\pi/3$ rotation of the vertical axis passing through the aligned hub atoms ($B_l B_u$) in the aligned bilayer gives rise to another stacking with sublattice alignment changed to ($A_l C_u$-$B_l B_u$-$C_l A_u$), where the two hub atoms (B_l and B_u) remain aligned and rim atoms' alignment is exchanged; this is called "hub-aligned" stacking. Similarly, a $\pi/3$ rotation along any of the aligned rim atoms ($A_l A_u$ or $C_l C_u$) of the aligned bilayer gives rise to different stackings where one of the aligned rim atoms remains unchanged and the hub atom and the second rim atom have mixed alignment ($A_l A_u$-$B_l C_u$-$C_l B_u$) or ($A_l C_u$-$B_l A_u$-$B_l B_u$); this is called "mixed" stacking. The two configurations of mixed stacking are equivalent structures as both rim atoms are equivalent. Additionally, sliding one of the layers in the aligned stacking for a distance a_0, which is the length between two sublattices, gives rise to the cyclic alignment of the sublattices ($A_l B_u$-$B_l C_u$-$C_l A_u$); this is called "cyclic" stacking. The discrete symmetries of all four bilayer stacking arrangements are discussed thoroughly in Ref. [46]. The single-layer of the dice lattice preserves the in-plane inversion symmetry with the interchange of two rim sites, which can be shown with the 3×3 matrix, W_0,

$$W_0 = \begin{pmatrix} 0 & 0 & 1 \\ 0 & 1 & 0 \\ 1 & 0 & 0 \end{pmatrix}. \quad (1)$$

In the case of the α-$\mathcal{T}_3$ lattice bilayer within the dice lattice limits, the aligned and hub-aligned stackings preserve in-plane inversion (W_1) and full inversion (W_2) symmetries with symmetry matrices $W_1 = \mathbb{1} \otimes W_0$ and $W_2 = \tau_x \otimes W_0$, where τ_x is the vector of the Pauli spin matrix defined in the layer space. W_1 and W_2 are 6×6 matrices which correspond to an interchange of rim sites in both planes and an additional interchange of layers, respectively. However, the cyclic stacking preserves only W_2 symmetry [46]. When $\alpha \neq 1$, for general

α-$\mathcal{T}_3$ cases, both W_1 and W_2 inversion symmetries are no longer preserved. The coupling between hub and rim atoms of different layers leads to particle-hole symmetry breaking in the case of mixed and cyclic stacking, as shown in later sections.

B. Tight-binding Hamiltonian

The tight-binding Hamiltonian for bilayer α-$\mathcal{T}_3$ lattice can be written as

$$
H = \sum_{m \in l, u} \left[\sum_{\langle i,j \rangle} t_{ij} C_i^{m\dagger} C_j^m + \sum_{\langle\langle i,j \rangle\rangle} t_{2i,j} e^{i\phi_{ij}^m} C_i^{m\dagger} C_j^m \right.
$$
$$
\left. + \sum_i \Delta_i C_i^{m\dagger} C_i^m + \text{H.c.} \right] + \left[\sum_{\langle p,q \rangle} t_{\perp p,q} C_p^{l\dagger} C_q^u + \text{H.c.} \right],
$$
(2)

where m is the layer index, which takes l (u) for the lower (upper) indices, and $C_i^{m\dagger}$ (C_i^m) is the creation (annihilation) operator of the ith site of layer m. We used $t = -1$ eV, $t_2 = 0.1t$, and $t_\perp = -0.4$ eV. The first term implies the NN hopping along directions $\boldsymbol{\delta_1} = (0, a_0)$, $\boldsymbol{\delta_2} = (-\frac{\sqrt{3}a_0}{2}, -\frac{a_0}{2})$, and $\boldsymbol{\delta_3} = (\frac{\sqrt{3}a_0}{2}, -\frac{a_0}{2})$ with strength t among A and B sublattices and αt among B and C sublattices. The second term is the complex next-nearest-neighbor (NNN) hopping (Haldane term) along the direction of the three vectors $\boldsymbol{v_1} = \boldsymbol{\delta_2} - \boldsymbol{\delta_3}$, $\boldsymbol{v_2} = \boldsymbol{\delta_3} - \boldsymbol{\delta_1}$, and $\boldsymbol{v_3} = \boldsymbol{\delta_1} - \boldsymbol{\delta_2}$, with hopping strength t_2 or αt_2 depending on the sublattices and phase ϕ_{ij}^m, which takes positive values for the electrons hopping clockwise and negative for anticlockwise hopping for each layer m. In the present work, we consider the Haldane phase to be same for both the layers as $\phi_{ij}^m = \phi_{ij}$. The NNN hopping from the B sublattice (hub atom) along that direction is forbidden due to the high potential barrier. The third term is the on-site energy term that takes positive and negative values for A_m and C_m sublattices, respectively. The last term in the Hamiltonian is the interlayer coupling term with coupling strength $t_\perp$. We consider $t_\perp$ to have the same values for coupling among different sublattices. The Fourier transform of the Hamiltonian [Eq. (2)] takes the form of

$$
H = \begin{pmatrix} H^l & H_c \\ H_c^T & H^u \end{pmatrix}.
$$
(3)

Here, H^l and H^u are 3×3 Hamiltonian matrices for the lower and upper layers, respectively, with the sublattice basis A_l, B_l, C_l for the bottom layer, and A_u, B_u, C_u for the top layer,

$$
H^l = H^u = \begin{pmatrix} f_z^+(k, t_2) & f(k, t) & 0 \\ f^*(k, t) & f_z^-(k, t_2) - f_z^-(k, \alpha t_2) & f(k, \alpha t) \\ 0 & f^*(k, \alpha t) & f_z^-(k, \alpha t_2) \end{pmatrix},
$$
(4)

and the general form of the coupling Hamiltonian

$$
H_c = \begin{pmatrix} t_\perp^{am} & t_\perp^c & t_\perp^h \\ 0 & t_\perp^{ah} & t_\perp^{mc} \\ t_\perp^{hc} & t_\perp^m & t_\perp^a \end{pmatrix},
$$
(5)

where $f_z^\pm(k, t_2') = f_1(k, t_2') \pm f_2(k, t_2')$ and $f(k, t') = f_x(k, t') - i f_y(k, t')$, and $t'(t_2')$ takes the values of either

$t(t_2)$ or $\alpha t(\alpha t_2)$,

$$
f_x(k, t') = t' \left\{ \cos a_0 k_y + 2 \cos \frac{\sqrt{3}a_0 k_x}{2} \cos \frac{a_0 k_y}{2} \right\},
$$

$$
f_y(k, t') = t' \left\{ \sin a_0 k_y - 2 \cos \frac{\sqrt{3}a_0 k_x}{2} \sin \frac{a_0 k_y}{2} \right\},
$$

$$
f_1(k) = 2t_2 \cos \phi \left\{ 2 \cos \frac{\sqrt{3}a_0 k_x}{2} \cos \frac{3a_0 k_y}{2} + \cos \sqrt{3}a_0 k_x \right\},
$$

$$
f_2(k) = \Delta - 2t_2 \sin \phi \left\{ 2 \sin \frac{\sqrt{3}a_0 k_x}{2} \cos \frac{3a_0 k_y}{2} \right.
$$
$$
\left. - \sin \sqrt{3}a_0 k_x \right\}.
$$

All the $t_\perp$ terms vanish except $t_\perp^{am}$, $t_\perp^{ah}$, and $t_\perp^a$ for the aligned case, $t_\perp^{hc}$, $t_\perp^{ah}$, and $t_\perp^h$ for the hub aligned, $t_\perp^{am}$, $t_\perp^m$, and $t_\perp^{mc}$ for the mixed, and $t_\perp^{hc}$, $t_\perp^c$, and $t_\perp^{mc}$ for the cyclic stacking cases, respectively. The magnitude of the interlayer coupling strength take values αt when hopping from the 'C' sublattices of any of the layer are considered. Hamiltonian H_l (H_u) for the lower (upper) layer in terms of spin-1 matrices is given as

$$
H_t = H_b = f_1(k)S_0 + f_2(k)S_z + f_x(k, t')S_x + f_y(k, t')S_y,
$$
(6)

where

$$
S_x = \begin{pmatrix} 0 & 1 & 0 \\ 1 & 0 & 1 \\ 0 & 1 & 0 \end{pmatrix}, \quad S_y = i \begin{pmatrix} 0 & -1 & 0 \\ 1 & 0 & -1 \\ 0 & 1 & 0 \end{pmatrix},
$$

$$
S_z = \begin{pmatrix} 1 & 0 & 0 \\ 0 & 0 & 0 \\ 0 & 0 & -1 \end{pmatrix}, \quad S_0 = \begin{pmatrix} 1 & 0 & 0 \\ 0 & 0 & 0 \\ 0 & 0 & 1 \end{pmatrix}.
$$

In the absence of NNN hopping, this Hamiltonian can be linearized for momentum around the Dirac points, taking the form of a pseudospin-1 Dirac-Weyl Hamiltonian [36],

$$
H_\xi(q) = \hbar v_f (\xi q_x S_x + q_y S_y),
$$
(7)

where $\mathbf{q} = \mathbf{k} - \mathbf{K}$ is the momentum around Dirac points, $\xi = \pm 1$ are the valley indices, and v_f is the Fermi velocity.

III. RESULTS AND DISCUSSION

A. Electronic spectrum

Now we discuss the energy spectrum of single-layer and bilayer α-$\mathcal{T}_3$ lattices of different stackings, obtained using the tight-binding Hamiltonian discussed above under the influence of Haldane flux. The band structures are calculated along the high-symmetry points: $\Gamma(0,0)$, $K(-\frac{4\pi}{3\sqrt{3}a_0}, \frac{2\pi}{3a_0})$, $M(0, \frac{2\pi}{3a_0})$, and $K'(\frac{4\pi}{3\sqrt{3}a_0}, \frac{2\pi}{3a_0})$ in the hexagonal Brillouin zone (BZ). In the single-layer α-$\mathcal{T}_3$ lattice, the three sublattices per unit cell result in three bands in the energy spectrum: one nondispersive flat band at zero energy and two conical bands from the valence band (VB) and conduction band (CB). All three bands intersect each other at K and K' with the flat band near the charge neutrality, similarly to graphene. We introduced the Haldane terms in the Hamiltonian and the threefold degeneracy is lifted, opening a gap at the Dirac points
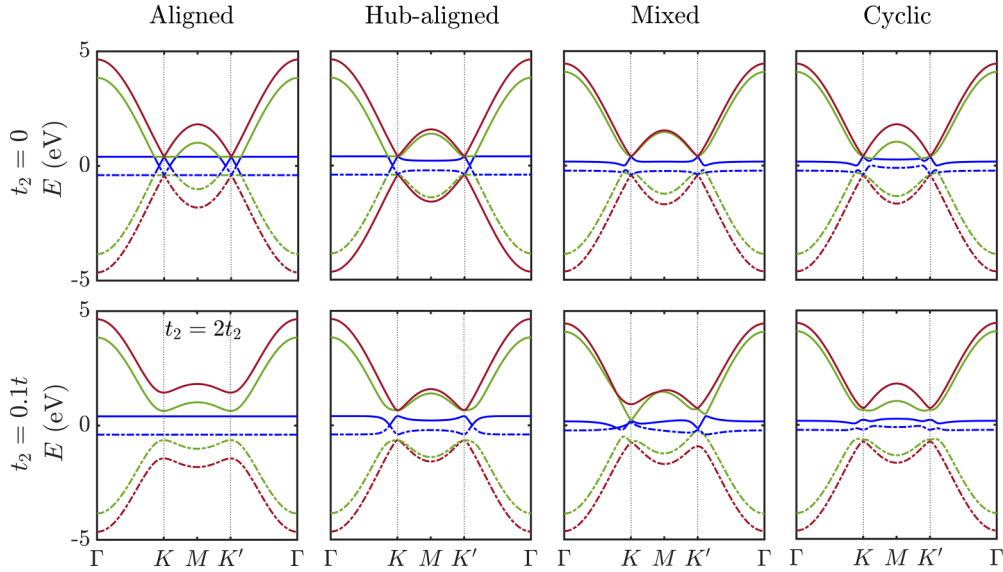
FIG. 2. Electronic band structure of all four nonequivalent commensurate stackings of bilayer α-$\mathcal{T}_3$ lattice, i.e., aligned (A_lA_u-B_lB_u-C_lC_u), hub-aligned (A_lC_u-B_lB_u-C_lC_u), mixed (A_lA_u-B_lC_u-C_lB_u), and cyclic (A_lB_u-B_lC_u-C_lA_u) for zero and nonzero values of t_2.

(K and K'), as shown in Fig. 10(a). Furthermore, we varied α from 1 to 0, which makes the flat bands more dispersive. It is worth noting that the flat band energy shows dispersion near the two Dirac points and remains nearly flat in the remaining high-symmetry path in the BZ. The bilayer α-$\mathcal{T}_3$ lattice's energy spectrum appears to be sensitive to the choice of the coupling strengths among the different sublattices of the two layers. All four nonequivalent commensurate stackings for the dice lattice limit ($\alpha = 1$) with and without the inclusion of the Haldane flux are shown in Fig. 2. In the bilayer geometry, the inclusion of the Haldane flux breaks TRS in all four stackings of the bilayer α-$\mathcal{T}_3$ lattice. Interestingly, particle-hole symmetry is preserved in aligned and hub-aligned stacking due to the hub-hub and rim-rim interlayer interactions, while it is broken in the mixed and cyclic stacking due to the presence of hub-rim interactions between the two layers. Furthermore, the low-energy bands dynamically change with increasing strengths of the NNN complex hopping strength (t_2), as shown in Fig. 3. These changes are symmetric at both the Dirac points (K and K'). In the case of aligned stacking, the valence and conduc-

tion bands degenerate at the Dirac point and around the Dirac points, while the flat bands are pushed away from zero energy. For a large value of NNN complex hopping strength (t_2), the degeneracy among all six bands is lifted, and the flat bands are around zero energy. Similarly to the single layer [45], the presence of NNN complex hopping strength (t_2) does not make them nontrivial, and their Chern numbers remain zero. In the hub-aligned and mixed stacking cases, the bands are strongly degenerate and are not separated with varying values of the NNN complex hopping strength (t_2). The most interesting case is the cyclic stacking of the bilayer α-$\mathcal{T}_3$ lattice. In this stacking, the conduction and valence bands are separated at charge neutrality with $t_2 = 0$, and all the bands become separated with the inclusion of Haldane flux with $t_2 = 0.1t$. The Haldane flux breaks the time-reversal symmetry of the system, and all six bands become separated, leaving a finite gap at zero energy, which makes the system insulating. The energy spectrum of cyclic stacking consists of two isolated, nearly flat bands near the Fermi level and four dispersive higher-energy bands, two in each conduction and valence band. The
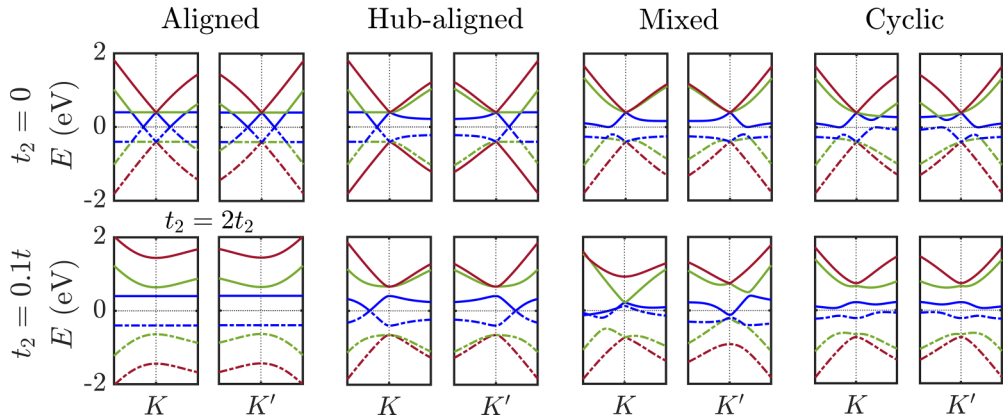

FIG. 3. Zoomed figure of the spectrum at the Dirac points K and K'. The dotted lines show the Fermi energy.

bandwidth of the two nearly flat bands (0.19 eV for valence and 0.21 eV for conduction) is found to decrease (0.16 eV for valence and 0.19 eV for conduction) for $t_2 = 0.1$ eV and becomes more flattened for $t_2 = 0.2$ eV. These flat bands are intriguing in a simple bilayer geometry when compared to complex systems like twisted bilayer graphene. Furthermore, we found that these flat bands are nontrivial, with nonzero Chern numbers, making the cyclic-stacked bilayer α-$\mathcal{T}_3$ lattice a potential candidate to study topological properties. Additionally, by changing the hopping strength αt [see Fig. 1(b)], the inversion symmetry is broken in the system, causing the two nearly flat bands to become dispersive.

B. Topological properties

Furthermore, we have conducted an extensive study of the cyclic stacking to investigate the topological properties of the bilayer α-$\mathcal{T}_3$ lattice. We calculated the Berry curvatures for the energy spectrum in the BZ for all six isolated bands and determined their respective Chern numbers. The z component of the Berry curvature was calculated numerically using [51]

$$\Omega_n(k_x, k_y) = -2 \sum_{n' \neq n} \text{Im} \left[\frac{\langle u_n | \frac{\partial H}{\partial k_x} | u_{n'} \rangle \langle u_{n'} | \frac{\partial H}{\partial k_y} | u_n \rangle}{(E_{n'} - E_n)^2} \right] \quad (8)$$

for the nth band for each k point, summing over all neighboring n' bands. Here, $|u_n\rangle$ are the block states, and E_n are the eigenvalues of the Hamiltonian given in Eq. (3) for the nth band. The surface integral of the Berry curvature over the first BZ yields $2\pi C_n$ for the nth band, where C_n is an integer called the Chern number or TKNN index [52,53]. The complex NNN hopping term plays a crucial role in determining the topological properties of the cyclic-stacked α-$\mathcal{T}_3$ bilayer lattice. In the bilayer cyclic α-$\mathcal{T}_3$ lattice, all six bands become topologically nontrivial. These include the flat bands VB1 and CB1, and the higher-energy dispersive bands VB2, VB3, CB2, and CB3 [see Fig. 1(c)]. We began from the dice lattice limit and varied α from 1 to 0 to observe the topological evolution in the system. At the dice lattice limit, the system becomes topological due to nonzero Chern numbers. VB1 (CB1), VB2 (CB2), and VB3 (CB3) possess Chern numbers of $+2$ (-2), $+3$ (-3), and $+1$ (-1), respectively. The continuous variation of α shows multiple phase transitions from one topological insulating phase to another through a band crossing between VB1 (CB1) and VB2 (CB2) in the valance (conduction) band at $\alpha = 0.58$ between the $\Gamma(M)$ and $K(K')$ point and at $\alpha = 0.608$ at the $K(K')$ point. After the transition, the nearly flat bands (VB1 and CB1) acquire very high Chern numbers of $C_n = \pm4$, while the middle bands (VB2 and CB2) acquires a chern number ±2. The Chern number of the lowest(highest) energy bands VB3 (CB3) changes from $+1(-1)$ to $+2(-2)$ due to a band crossings between VB3 (CB3) and VB2 (CB2) at the Dirac point $K(K')$. Figures 4(a) and 4(b) show the dispersive nearly flat band structures for three different values of α aside from 1. The red dashed curve shows the band crossing in both Figs. 4(a) and 4(b). Figures 4(c) and 4(d) show the Chern number line plots as a function of α for all six bands, clearly showing the switching of Chern numbers at the transition points. This behaviour of multiple phase transition is not observed for its single-layer counterpart in the presence
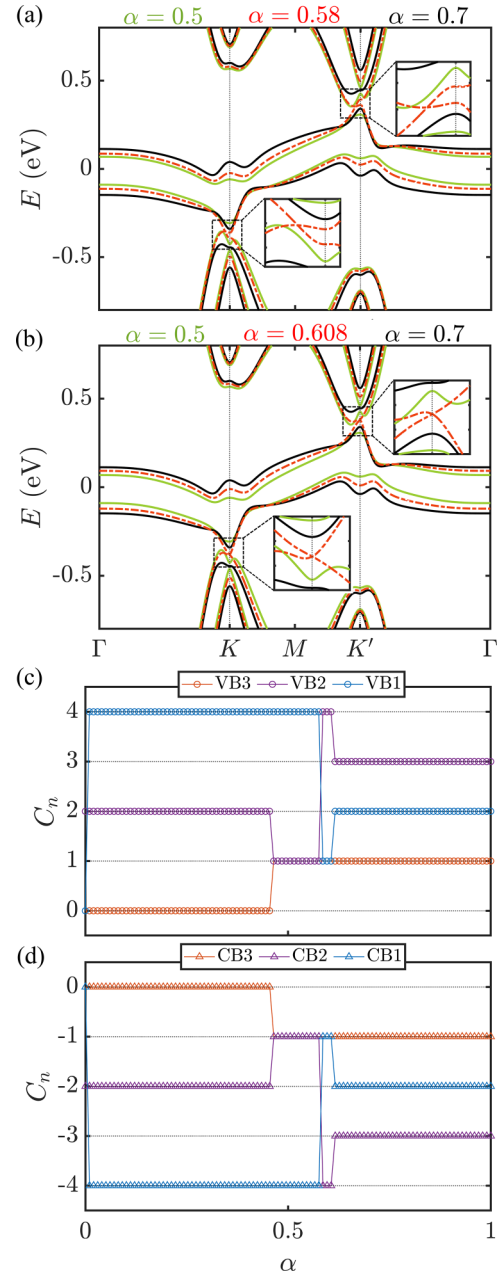

FIG. 4. Band structure of cyclic bilayer α-$\mathcal{T}_3$ for different values of α showing band closing and opening for phase transition in the VB (CB) (a) between $\Gamma(M)$ and $K(K')$, $\alpha = 0.5$ (green), $\alpha = 0.58$ (red) and $\alpha = 0.7$ (black); (b) at $K(K')$, $\alpha = 0.5$ (green), $\alpha = 0.608$ (red) and $\alpha = 0.7$ (black). For all three cases we use $t_2 = 0.1t$, $\phi = \frac{\pi}{2}$, $\Delta = 0$. The bands are no longer symmetric under the exchange of valley for $\alpha \neq 1$. (c) The variation of Chern number as a function of α for three (c) VB and (d) CB.

of the Haldane term. However, a similar study of topological phase transition has been observed for the single-layer α-$\mathcal{T}_3$ lattice when irradiated with off-resonant circularly polarized light [43] or using intrinsic spin-orbit coupling [1]. The variation in α breaks the W_2 inversion symmetry, as visualized in the Berry curvature distribution shown in Fig. 5. The Berry curvature distribution over the k_x-k_y plane at the dice lattice limit ($\alpha = 1$) exhibits the same features at the K and K' points,
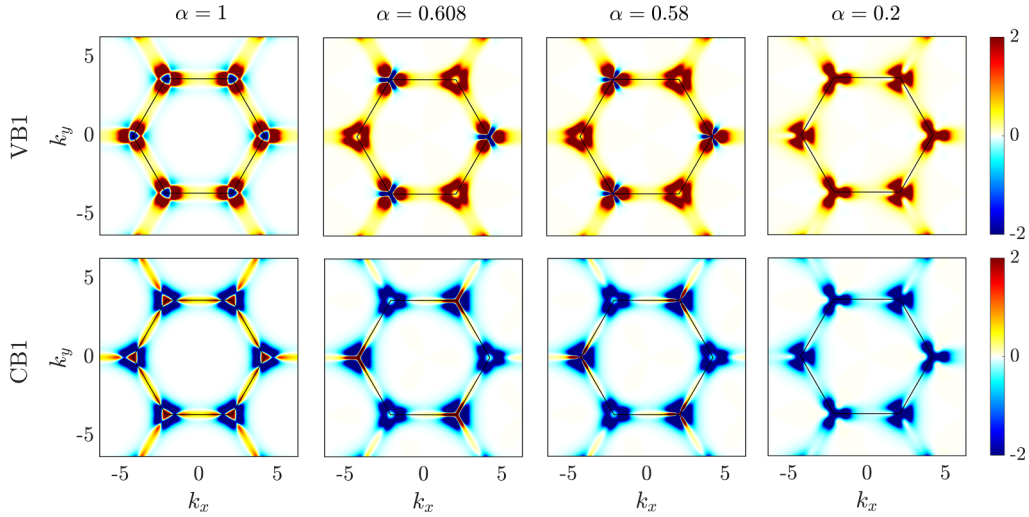
FIG. 5. Berry curvature distribution in the k_x-k_y plane for the nearly flat valance (VB1) and conduction (CB1) bands for $\alpha = 1$ (dice lattice limit), 0.608, 0.58, and $\alpha = 0.2$. Here t_2, Δ, and ϕ are fixed at $0.1t$, 0, and $\frac{\pi}{2}$, respectively.

reflecting the preserved W_2 inversion symmetry in the system. For α values other than 1, the symmetry breaks, resulting in different Berry curvature distributions at K and K'.

C. Chern phase diagrams

The bilayer cyclic α-$\mathcal{T}_3$ lattice exhibits a rich interplay between time-reversal and inversion asymmetry controlled by the flux phase ϕ and the parameter α, respectively. The simultaneous variation of ϕ and α gives rise to a multitude of new topological phases. In Fig. 4, we demonstrate how the Chern insulating phase evolves as we fix $\phi = \frac{\pi}{2}$ while varying α. However, there is more to explore within the parameter space $0 < \phi < \pi$. Our investigations reveal additional Chern phases, which we have summarized in the Chern number phase diagram shown in Fig. 6. Here, we examine the dependencies of the Chern numbers for VB1 (CB1), VB2 (CB2), and VB3 (CB3) on α and ϕ. Here we change
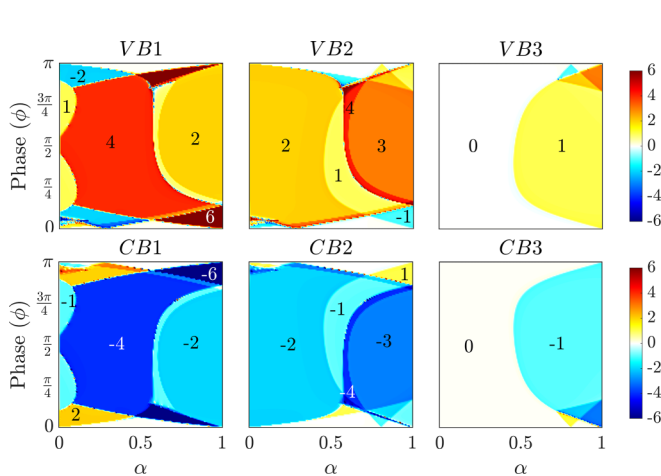
the Haldane phase for both layers simultaneously. Notably, the Chern numbers of the lower energy valance/conduction bands exhibit sensitivity to both α and ϕ. Meanwhile, the second set of dispersive bands (VB3 and CB3) displays a negligible dependence on ϕ within a very small range. In the phase diagram, we also present the conventional Haldane phase diagram (see Fig. 7) for the nearly flat valence band (VB1) and conduction band (CB1). This diagram depicts the Chern number as a function of Δ and ϕ for specific values of α. Also, we have shown the sinusoidal phase boundary separating the trivial and topological phase for the ordinary Haldane model of graphene, $\Delta = \pm 3\sqrt{3}t_2 \sin \phi$, with a black curve [54]. It is essential to note that for intermediate values of α when the flat bands become dispersive, the topological phase depends on the NNN neighbor hopping strength t_2 (see Fig. 8). We illustrate this by displaying the Chern number plots as a function of α for band VB3 with varying values of t_2.
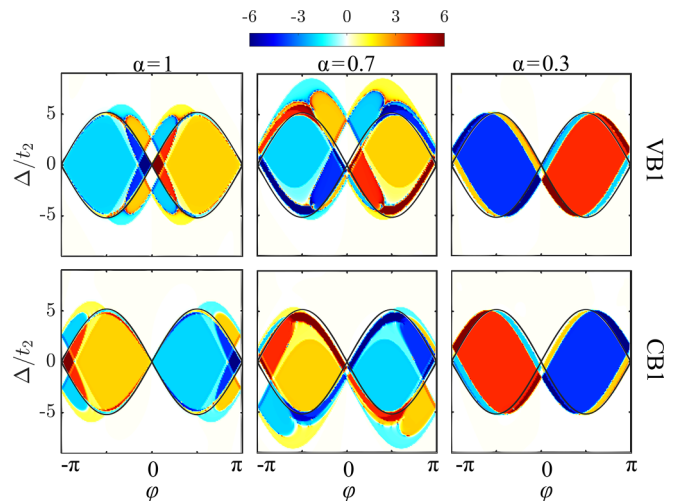

FIG. 6. Chern number phase diagram of three valance bands (top row) and conduction bands (bottom row) of cyclic bilayer α-$\mathcal{T}_3$ lattice in the parameter space α ($0 \sim 1$) and ϕ ($0 \sim \pi$). $t_2 = 0.1t$, $\Delta = 0$ for all bands.

FIG. 7. The Haldane phase diagram shown for VB1 ($n = 3$) and CB1 ($n = 4$) for different values of α along with the sinusoidal Haldane phase boundary (black curve).
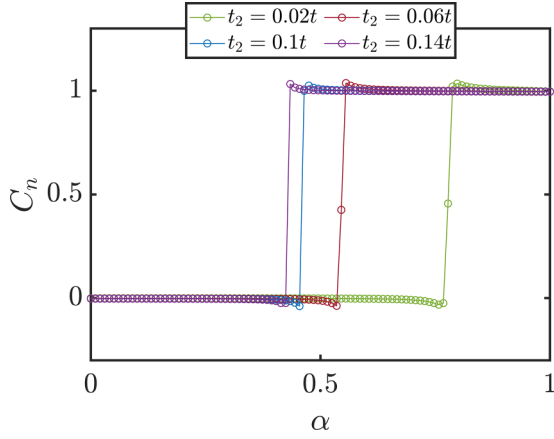
FIG. 8. Chern number variation of VB1 ($n = 3$) with α for different values of NNN hopping parameter t_2. We kept $\Delta = 0$ and $\phi = \frac{\pi}{2}$ here.

For instance, when $t_2 = 0.06t$ eV, we observe a Chern number phase transition from $|C| = 0$ to $|C| = 1$ at $\alpha = 0.545$, leading to a smaller $C = 1$ region in the Chern number phase diagram compared to $t_2 = 0.1t$ in Fig. 6, irrespective of the value of ϕ. As we increase t_2, the transition occurs at lower values of α.

D. Anomalous Hall conductivity

In this section, we calculate the anomalous Hall conductivity for the bilayer cyclic α-$\mathcal{T}_3$ lattice. This conductivity, a measure of how electrons respond to an external electric field, can provide insights into the topological properties of the material. We compute the Hall conductivity by numerically integrating the Berry curvature of all occupied electronic states over the entire BZ. This involves summing up contributions from all the bands in the material [51],

$$\sigma_{xy} = \frac{\sigma_0}{2\pi} \sum_n \int \Omega_n(k_x, k_y) f\left(E^n_{k_x,k_y}\right) dk_x dk_y, \qquad (9)$$

where Ω_n is the Berry curvature for the nth band from Eq. (7), $f(E) = 1/[1 + e^{(E-E_f)/K_B T}]$ is the Fermi-Dirac distribution function where E_f and T signify Fermi energy and absolute temperature, $E^n_{k_x,k_y}$ are the energy eigenvalues for the nth band, and $\sigma_0 = e^2/h$. The anomalous Hall conductivity arises due to the nonzero Berry curvature contributions of all occupied states. As the Fermi energy lies in a band gap, the Fermi-Dirac distribution function $f(E)$ at zero absolute temperature is 1, and the total contribution of all occupied states comes from bands below the Fermi energy. Then the integration over the BZ gives the total Chern number of the bands below the Fermi energy and we get a plateau $\sigma_{xy} = |C_n|e^2/h$. The conductivity decays when the Fermi energy lies outside of the gap. The anomalous Hall conductivity (AHC) for this system at the $\alpha = 1$ limit is plotted as a function of Fermi energy (E_f) in units of σ_0 as shown in Fig. 9(a). From the AHC we noticed three different plateau regions with respect to the Fermi energies. As we move the Fermi energy from zero energy to higher values to the gap between VB1 and VB2, the AHC is solely contributed by the VB3 ($C_n = 1$) and VB2 ($C_n = 3$), resulting in $\sigma_{xy} = |4|e^2/h$, and the total
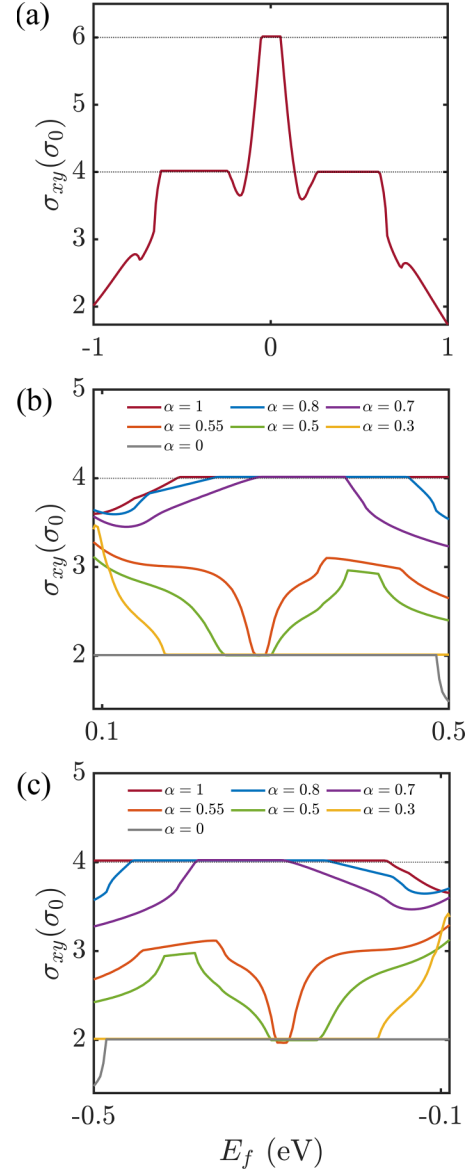

FIG. 9. The Hall conductivity depicted as a function of Fermi energy, E_f (a) for $\alpha = 1$, for several values of α for (b) Fermi energy near CB phase transition and (c) Fermi energy near VB phase transition, the other parameters taken as $t_2 = 0.1t$, $\phi = \pi/2$, $\Delta = 0$.

Chern number $C_n = 4$ is just some of the two Chern numbers of VB3 and VB2. We see from the plot a plateau at $4e^2/h$ remains quantized within the gap. Similarly, we observe another plateau at $4e^2/h$ for the energy gap between CB2 and CB1 as the Chern number of VB1 and CB1 being $+2$ and -2; the total Chern number remains 4. The system attains its maximum conductivity when the Fermi energy lies in the gap between VB1 and CB1. For the Fermi energy lying in this region, the total Chern number of all the bands below the Fermi energy is 6 and we see a plateau at $6e^2/h$. The asymmetry in the plot arises due to the particle-hole asymmetry present in the cyclic bilayer system. In order to visualize the nature of AHC plateaus after the phase transition, we have depicted the Hall conductivity for several values of α, for Fermi energies near the CB and VB phase transition point, i.e., E_f lying in the
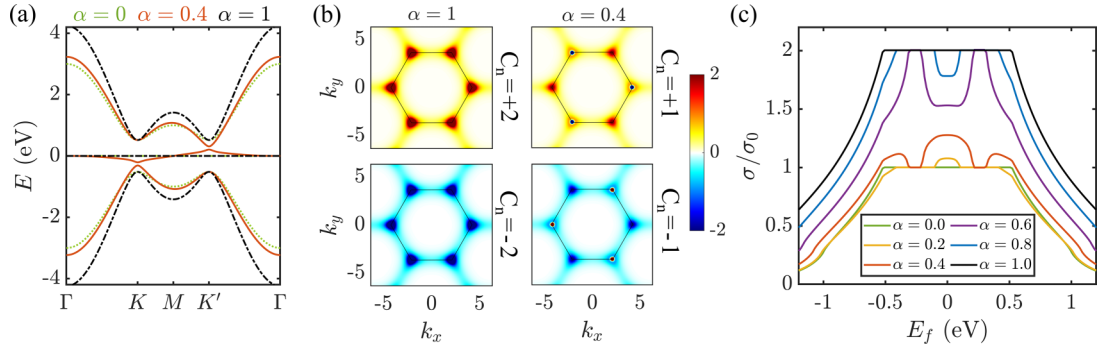
FIG. 10. Single layer α-$\mathcal{T}_3$ (a) spectrum for $\alpha = 1$ (black) and $\alpha = 0.4$ (blue) and $\alpha = 0$ (green), (b) Berry curvature for bands corresponding to the Chern number $+2$ (VB) and -2 (CB) for $\alpha = 1$, and $+1$ (VB) and -1 (CB) for $\alpha = 0.4$ are presented. (c) Anomalous hall conductivity is shown for various values of α, which are indicated in the inset. The values of t_2, ϕ, Δ are taken as $0.1t$, $\pi/2$ and zero respectively.

gap between CB1, CB2 and VB1, VB2, respectively. As we have discussed before (see Fig. 4), a topological phase transition accompanied by a band closure and opening is observed by changing hopping strength using α for both VB in the energy range (0.3 eV - 0.5 eV) and (-0.5 eV - -0.3 eV), respectively. And for the Fermi energy in any of the gaps mentioned above, we see a conductivity plateau at $4e^2/h$. As we lower the value of α, this plateau gradually diminishes as the gap becomes narrower and completely vanishes at the transition point when the band gap closes, and eventually, we see a new plateau arising at $2e^2/h$ as the gap opens again. The new plateau at $2e^2/h$ arises because the Chern numbers associated with both the band changes after the transitions leading to the total Chern number of the bands below the Fermi energy always being $C_T = 2$ for both VB and CB. Figures 9(b) and 9(c) show the conductivity for Fermi energies near the transition point for CB and VB, respectively, for different α values.

IV. CONCLUSION

We introduced the Haldane model for four nonequivalent vertically aligned commensurate stackings for a bilayer α-$\mathcal{T}_3$ lattice in the Dice lattice limit. We found that both aligned and cyclic stackings open up a band gap when the TRS is broken and the gap depends on both t_2 and interlayer coupling. We investigated the topological properties of cyclic stacking within the tight-binding formalism. The cyclic stacking has all six bands topologically nontrivial including two nearly flat bands with a higher Chern number, $C_n = \pm 3$. Further, we allowed the variation of α starting from the Dice lattice limit and observed multiple topological phase transitions in the valance band and the conduction band for different values of α. The phase transition occurs at the gap closing between VB1 and VB2 in the valance band and CB1 and CB2 in the conduction band, while the third band becomes trivial. The partial flat bands acquire a Chern number as high as $C_n = \pm 4$ after the transition. We obtained the phase diagram in the parameter space α and ϕ for all six bands that exhibit multiple Chern phase regions. A higher Chern number arises for the low energy bands and a trivial region arises for higher energy bands. We also calculated the anomalous Hall conductivity for the Dice lattice limit as well as for different

α values for Fermi energy close to the transition point. The conductivity plateau shows a jump from $4e^2/h$ to $2e^2/h$ which supports the phase transition from one Chern insulating phase to another.

APPENDIX: SINGLE-LAYER α-$\mathcal{T}_3$ FOR $\alpha \neq 1$

Here we discuss in more detail the effect of broken inversion symmetry in the presence of Haldane flux in a single-layer α-$\mathcal{T}_3$ Hamiltonian [Eq. (4)] and the fate of topological bands and anomalous Hall conductivity as we evolve the hopping strength between sites B and C [Fig. 1(a)] using the real parameter α. The single layer α-$\mathcal{T}_3$ lattice preserves the W_0 inversion symmetry in the dice lattice limit. For α values $\neq 0, 1$ the inversion symmetry breaks. Introducing Haldane flux breaks time-reversal symmetry, Kramer's degeneracy is lifted, and the energy becomes an odd function of k as can be seen for the red curve ($\alpha = 0.4$) in the spectrum of Fig. 10(a). The Berry curvature plots for the VB and CB (as shown in Fig. 10(b)) show different values at K and $-K$ for $\alpha \neq 1$ showing the inversion symmetry breaking in the system. Though the middle band becomes dispersive and acquires a finite Berry curvature value, the total Berry curvature over BZ is zero and the band remains trivial in nature. Figure 10(c) presents the Hall conductivity as a function of Fermi energy for various values of α. $\alpha = 1$ corresponds to a completely flat middle band and this band has no contribution to the Berry curvature integral which leads to a Hall conductivity plateau at $2\sigma_0$ when E_f lies in the gap. When $\alpha \neq 1$ the dispersive middle band has a finite contribution to the Berry curvature integral and it reduces the overall contributions of

all occupied states and we see a dip around zero energy. As the middle band becomes more dispersive with α values

away from 1, we see a broader and deeper dip in the Hall conductivity.

[1] J. Wang and J.-F. Liu, Quantum spin hall phase transition in the $\alpha - T_3$ lattice, Phys. Rev. B **103**, 075419 (2021).

[2] H. Liu, S. Meng, and F. Liu, Screening two-dimensional materials with topological flat bands, Phys. Rev. Mater. **5**, 084203 (2021).

[3] S. Javvaji, J.-H. Sun, and J. Jung, Topological flat bands without magic angles in massive twisted bilayer graphenes, Phys. Rev. B **101**, 125411 (2020).

[4] M. Yankowitz, J. Jung, E. Laksono, N. Leconte, B. L. Chittari, K. Watanabe, T. Taniguchi, S. Adam, D. Graf, and C. R. Dean, Dynamic band-structure tuning of graphene moiré superlattices with pressure, Nature (London) **557**, 404 (2018).

[5] H. Kim, N. Leconte, B. L. Chittari, K. Watanabe, T. Taniguchi, A. H. MacDonald, J. Jung, and S. Jung, Accurate gap determination in monolayer and bilayer graphene/*h*-BN moiré superlattices, Nano Lett. **18**, 7732 (2018).

[6] B. L. Chittari, G. Chen, Y. Zhang, F. Wang, and J. Jung, Gate-tunable topological flat bands in trilayer graphene boron-nitride moiré superlattices, Phys. Rev. Lett. **122**, 016401 (2019).

[7] G. Chen, L. Jiang, S. Wu, B. Lyu, H. Li, B. L. Chittari, K. Watanabe, T. Taniguchi, Z. Shi, J. Jung, Y. Zhang, and F. Wang, Evidence of a gate-tunable Mott insulator in a trilayer graphene moiré superlattice, Nat. Phys. **15**, 237 (2019).

[8] N. R. Chebrolu, B. L. Chittari, and J. Jung, Flat bands in twisted double bilayer graphene, Phys. Rev. B **99**, 235417 (2019).

[9] Y. Park, B. L. Chittari, and J. Jung, Gate-tunable topological flat bands in twisted monolayer-bilayer graphene, Phys. Rev. B **102**, 035411 (2020).

[10] S. Sinha, P. C. Adak, R. S. Surya Kanthi, B. L. Chittari, L. D. V. Sangani, K. Watanabe, T. Taniguchi, J. Jung, and M. M. Deshmukh, Bulk valley transport and Berry curvature spreading at the edge of flat bands, Nat. Commun. **11**, 5548 (2020).

[11] J. Shin, Y. Park, B. L. Chittari, J.-H. Sun, and J. Jung, Electron-hole asymmetry and band gaps of commensurate double moire patterns in twisted bilayer graphene on hexagonal boron nitride, Phys. Rev. B **103**, 075423 (2021).

[12] D. A. G. González, B. L. Chittari, Y. Park, J.-H. Sun, and J. Jung, Topological phases in *N*-layer ABC graphene/boron nitride moiré superlattices, Phys. Rev. B **103**, 165112 (2021).

[13] J. Shin, B. L. Chittari, and J. Jung, Stacking and gate-tunable topological flat bands, gaps, and anisotropic strip patterns in twisted trilayer graphene, Phys. Rev. B **104**, 045413 (2021).

[14] J. Shin, B. L. Chittari, Y. Jang, H. Min, and J. Jung, Nearly flat bands in twisted triple bilayer graphene, Phys. Rev. B **105**, 245124 (2022).

[15] N. R. Chebrolu and B. L. Chittari, Analytical model of the energy spectrum and Landau levels of a twisted double bilayer graphene, Physica E **146**, 115526 (2023).

[16] Y. Park, Y. Kim, B. L. Chittari, and J. Jung, Topological flat bands in rhombohedral tetralayer and multilayer graphene on hexagonal boron nitride moiré superlattices, Phys. Rev. B **108**, 155406 (2023).

[17] S. Miyahara, S. Kusuta, and N. Furukawa, BCS theory on a flat band lattice, Physica C: Superconductivity **460-462**, 1145 (2007).

[18] D. Jérome, T. M. Rice, and W. Kohn, Excitonic insulator, Phys. Rev. **158**, 462 (1967).

[19] G. Sethi, Y. Zhou, L. Zhu, L. Yang, and F. Liu, Flat-band-enabled triplet excitonic insulator in a diatomic kagome lattice, Phys. Rev. Lett. **126**, 196403 (2021).

[20] E. Tang, J.-W. Mei, and X.-G. Wen, High-temperature fractional quantum Hall states, Phys. Rev. Lett. **106**, 236802 (2011).

[21] T. Neupert, L. Santos, C. Chamon, and C. Mudry, Fractional quantum Hall states at zero magnetic field, Phys. Rev. Lett. **106**, 236804 (2011).

[22] K. Sun, Z. Gu, H. Katsura, and S. Das Sarma, Nearly flatbands with nontrivial topology, Phys. Rev. Lett. **106**, 236803 (2011).

[23] E. C. Stoner, Collective electron ferromagnetism, Proc. R. Soc. London A **165**, 372 (1938).

[24] W. Jiang, H. Huang, and F. Liu, A Lieb-like lattice in a covalent-organic framework and its Stoner ferromagnetism, Nat. Commun. **10**, 2207 (2019).

[25] Y. Zhou, G. Sethi, H. Liu, Z. Wang, and F. Liu, Excited quantum anomalous and spin Hall effect: Dissociation of flat-bands-enabled excitonic insulator state, Nanotechnol. **33**, 415001 (2022).

[26] K. Ohgushi, S. Murakami, and N. Nagaosa, Spin anisotropy and quantum Hall effect in the kagomé lattice: Chiral spin state based on a ferromagnet, Phys. Rev. B **62**, R6065 (2000).

[27] H.-M. Guo and M. Franz, Topological insulator on the kagome lattice, Phys. Rev. B **80**, 113102 (2009).

[28] B. Sutherland, Localization of electronic wave functions due to local topology, Phys. Rev. B **34**, 5208 (1986).

[29] J. Vidal, R. Mosseri, and B. Douçot, Aharonov-Bohm cages in two-dimensional structures, Phys. Rev. Lett. **81**, 5888 (1998).

[30] C. Weeks and M. Franz, Topological insulators on the Lieb and perovskite lattices, Phys. Rev. B **82**, 085310 (2010).

[31] N. Goldman, D. F. Urban, and D. Bercioux, Topological phases for fermionic cold atoms on the Lieb lattice, Phys. Rev. A **83**, 063601 (2011).

[32] L. Zheng, L. Feng, and W. Yong-Shi, Exotic electronic states in the world of flat bands: From theory to material, Chin. Phys. B **23**, 077308 (2014).

[33] J.-W. Rhim and B.-J. Yang, Classification of flat bands according to the band-crossing singularity of Bloch wave functions, Phys. Rev. B **99**, 045107 (2019).

[34] D. L. Bergman, C. Wu, and L. Balents, Band touching from real-space topology in frustrated hopping models, Phys. Rev. B **78**, 125104 (2008).

[35] M. Rizzi, V. Cataudella, and R. Fazio, Phase diagram of the Bose-Hubbard model with $\mathcal{T}_3$ symmetry, Phys. Rev. B **73**, 144511 (2006).

[36] D. Bercioux, D. F. Urban, H. Grabert, and W. Häusler, Massless Dirac-Weyl fermions in a $\mathcal{T}_3$ optical lattice, Phys. Rev. A **80**, 063603 (2009).

[37] F. Wang and Y. Ran, Nearly flat band with Chern number $C = 2$ on the dice lattice, Phys. Rev. B **84**, 241103(R) (2011).

[38] E. Illes, J. P. Carbotte, and E. J. Nicol, Hall quantization and optical conductivity evolution with variable Berry phase in the α-T_3 model, Phys. Rev. B **92**, 245410 (2015).

[39] A. Raoux, M. Morigi, J.-N. Fuchs, F. Piéchon, and G. Montambaux, From dia- to paramagnetic orbital susceptibility of massless fermions, Phys. Rev. Lett. **112**, 026402 (2014).

[40] T. Biswas and T. K. Ghosh, Magnetotransport properties of the α-T_3 model, J. Phys.: Condens. Matter **28**, 495302 (2016).

[41] J. J. Wang, S. Liu, J. Wang, and J.-F. Liu, Integer quantum Hall effect of the α-T_3 model with a broken flat band, Phys. Rev. B **102**, 235414 (2020).

[42] B. Dey and T. K. Ghosh, Photoinduced valley and electron-hole symmetry breaking in α-T_3 lattice: The role of a variable Berry phase, Phys. Rev. B **98**, 075422 (2018).

[43] B. Dey and T. K. Ghosh, Floquet topological phase transition in the α-$\mathcal{T}_3$ lattice, Phys. Rev. B **99**, 205429 (2019).

[44] B. Dey, P. Kapri, O. Pal, and T. K. Ghosh, Unconventional phases in a Haldane model of dice lattice, Phys. Rev. B **101**, 235406 (2020).

[45] S. Mondal and S. Basu, Topological features of the Haldane model on a dice lattice: Flat-band effect on transport properties, Phys. Rev. B **107**, 035421 (2023).

[46] P. O. Sukhachov, D. O. Oriekhov, and E. V. Gorbar, Stackings and effective models of bilayer dice lattices, Phys. Rev. B **108**, 075166 (2023).

[47] S. E. Korshunov, Vortex ordering in fully frustrated superconducting systems with a dice lattice, Phys. Rev. B **63**, 134503 (2001).

[48] D. F. Urban, D. Bercioux, M. Wimmer, and W. Häusler, Barrier transmission of Dirac-like pseudospin-one particles, Phys. Rev. B **84**, 115136 (2011).

[49] J. D. Malcolm and E. J. Nicol, Frequency-dependent polarizability, plasmons, and screening in the two-dimensional pseudospin-1 dice lattice, Phys. Rev. B **93**, 165433 (2016).

[50] M. Vigh, L. Oroszlány, S. Vajna, P. San-Jose, G. Dávid, J. Cserti, and B. Dóra, Diverging dc conductivity due to a flat band in a disordered system of pseudospin-1 Dirac-Weyl fermions, Phys. Rev. B **88**, 161413(R) (2013).

[51] D. Xiao, M.-C. Chang, and Q. Niu, Berry phase effects on electronic properties, Rev. Mod. Phys. **82**, 1959 (2010).

[52] D. J. Thouless, M. Kohmoto, M. P. Nightingale, and M. den Nijs, Quantized Hall conductance in a two-dimensional periodic potential, Phys. Rev. Lett. **49**, 405 (1982).

[53] J. E. Avron, R. Seiler, and B. Simon, Homotopy and quantization in condensed matter physics, Phys. Rev. Lett. **51**, 51 (1983).

[54] F. D. M. Haldane, Model for a quantum Hall effect without Landau levels: Condensed-matter realization of the "parity anomaly", Phys. Rev. Lett. **61**, 2015 (1988).